

Thermo-fluid-dynamics of natural convection around a heated vertical plate with a critical assessment of the standard similarity theory

Abhijit Guha, and Subhajit Nayek

Citation: [Physics of Fluids](#) **29**, 103607 (2017);

View online: <https://doi.org/10.1063/1.4990279>

View Table of Contents: <http://aip.scitation.org/toc/phf/29/10>

Published by the [American Institute of Physics](#)

Articles you may be interested in

[Turbulent kinetic energy budget in the boundary layer developing over an urban-like rough wall using PIV](#)
[Physics of Fluids](#) **29**, 085113 (2017); 10.1063/1.4997205

[Heat transport and coupling modes in Rayleigh–Bénard convection occurring between two layers with largely different viscosities](#)
[Physics of Fluids](#) **29**, 096602 (2017); 10.1063/1.4989592

[Origin of the onset of Rayleigh–Bénard convection in a concentrated suspension of microgels with a yield stress behavior](#)
[Physics of Fluids](#) **29**, 104102 (2017); 10.1063/1.4995699

[Convective heat transfer in non-uniformly heated corrugated slots](#)
[Physics of Fluids](#) **29**, 103605 (2017); 10.1063/1.4989686

[Kolmogorov's Lagrangian similarity law revisited](#)
[Physics of Fluids](#) **29**, 105106 (2017); 10.1063/1.4993834

[Exact and approximate solutions for transient squeezing flow](#)
[Physics of Fluids](#) **29**, 103606 (2017); 10.1063/1.4999071



**COMPLETELY
REDESIGNED!**



**PHYSICS
TODAY**

Physics Today Buyer's Guide
Search with a purpose.

Thermo-fluid-dynamics of natural convection around a heated vertical plate with a critical assessment of the standard similarity theory

Abhijit Guha^{a)} and Subhajit Nayek

Mechanical Engineering Department, Indian Institute of Technology Kharagpur, Kharagpur 721302, India

(Received 14 June 2017; accepted 20 September 2017; published online 27 October 2017)

A compulsory element of all textbooks on natural convection has been a detailed similarity analysis for laminar natural convection on a heated semi-infinite vertical plate and a routinely used boundary condition for such analysis is $u = 0$ at $x = 0$. The same boundary condition continues to be assumed in related theoretical analyses, even in recent publications. The present work examines the consequence of this long-held assumption, which appears to have never been questioned in the literature, on the fluid dynamics and heat transfer characteristics. The assessment has been made here by solving the Navier-Stokes equations numerically with two boundary conditions—one with constrained velocity at $x = 0$ to mimic the similarity analysis and the other with no such constraints simulating the case of a heated vertical plate in an infinite expanse of the quiescent fluid medium. It is found that the fluid flow field given by the similarity theory is drastically different from that given by the computational fluid dynamics (CFD) simulations with unconstrained velocity. This also reflects on the Nusselt number, the prediction of the CFD simulations with unconstrained velocity being quite close to the experimentally measured values at all Grashof and Prandtl numbers (this is the first time theoretically computed values of the average Nusselt number \overline{Nu} are found to be so close to the experimental values). The difference of the Nusselt number ($\Delta\overline{Nu}$) predicted by the similarity theory and that by the CFD simulations (as well as the measured values), both computed with a high degree of precision, can be very significant, particularly at low Grashof numbers and at Prandtl numbers far removed from unity. Computations show that within the range of investigations ($10^4 \leq Gr_L \leq 10^8$, $0.01 \leq Pr \leq 100$), the maximum value of $\Delta\overline{Nu}$ may be of the order 50%. Thus, for quantitative predictions, the available theory (i.e., similarity analysis) can be rather inadequate. With the help of the CFD simulations, the details of the fluid dynamics, particularly the physics of fluid entrainment, are thoroughly studied. It is shown that the relative proportions of the fluid entrainment from the bottom, top, and side of the vertical plate depend on the size of the region of interest (ROI). As the size of the ROI is made large, most of the entrained fluid comes from the bottom, a little bit from the top and almost no fluid enters from the side; the nature of entrainment is opposite in the similarity analysis for which all the fluid enters from the side and no fluid enters either from the bottom or the top. The two sets of CFD simulations establish, in particular, the conclusion that it is the inappropriateness of the age-old boundary condition $u = 0$ at $x = 0$, and not the boundary layer approximation, that is the principal cause for the vulnerability of the standard similarity analyses (and integral theories) for natural convection. The CFD solutions further demonstrate the effects of finite length and finite thickness of the plate on the flow field and the shape of the buoyant jet. The different boundary conditions on the two sides of the vertical plate and the presence of its finite thickness make the buoyant jet bend over the top edge of the plate and make the evolution of entrainment from the two sides of the free buoyant jet different. The entrainment velocity from the two sides, however, equilibrates at a certain distance above the plate. The asymmetry in the velocity and temperature fields above the plate decreases more rapidly when Pr is smaller and Gr_L is greater. It is shown that sufficiently above the plate, the distributions of axial velocity and temperature in the buoyant jet tend to be symmetric with respect to an axis that seems to pass through the vertical mid-plane of the plate, i.e., the jet tends to lose its history of origination. *Published by AIP Publishing.*
<https://doi.org/10.1063/1.4990279>

I. INTRODUCTION

Natural convection is a widespread natural phenomenon where convective motion is naturally set up in a fluid body as a

result of the establishment of a temperature difference. Its analysis is complex because the velocity scale is not imposed but arises from the simultaneous solution of coupled differential equations representing the conservation of mass, momentum, and energy. One of the most fundamental and popular analyses involves the derivation of self-similar solutions for natural convection on an isothermally heated semi-infinite vertical plate,

^{a)}Author to whom correspondence should be addressed: a.guha@mech.iitkgp.ernet.in

and this topic is a compulsory element of all textbooks on natural convection.^{1–5} The present paper also concerns this topic but the power of computational fluid dynamics (CFD) is invoked here to unravel the detailed thermo-fluid-dynamics of the phenomenon. The CFD solutions create a comprehensive physical understanding both in qualitative and quantitative aspects, not available previously, and offer a route to precisely assess the accuracy (or applicability) of previous theoretical solutions which are usually derived under more restrictive assumptions. As an example, a routinely used boundary condition for the similarity analysis of natural convection over a vertical flat plate is $u = 0$ at $x = 0$. The present work examines the consequence of this long-held assumption, which appears to have never been questioned in the literature, on the fluid dynamics and heat transfer characteristics. The assessment has been made here by solving the Navier-Stokes equations numerically with two boundary conditions—one with constrained velocity at $x = 0$ to mimic the similarity analysis and the other with no such constraints simulating the case of a heated vertical plate in an infinite expanse of the quiescent fluid medium. For a focussed discussion, the main text is concerned with an isothermal vertical plate, while the constant heat flux case is discussed in the [Appendix](#) for the sake of completeness. The robustness of the present approach is founded on the computational experience drawn from a recent study of natural convection above a heated horizontal plate.⁶

Laminar natural convection on a vertical plate has been studied by experiments,^{7–12} similarity theory,^{13,14} and integral theories.¹⁵ According to Saunders,⁷ the history of publication on the study of natural convection over a vertical plate goes back to 1881 when Lorenz¹⁶ tackled the problem but incorrectly deduced that the iso-velocity and iso-temperature surfaces are formed parallel to the plate. According to Rich and Burbank,⁹ Pohlhausen was the first to extend in 1921 the Blasius solution by including heat transfer, i.e., the energy equation in the boundary layer analysis (although Rich and Burbank did not specify the actual publication, we could locate this first similarity analysis of forced convection heat transfer, Ref. 17). We could find the first presentation of the similarity solution for the natural convection problem in the paper by Schmidt and Beckmann¹³ published in November 1930. [As an interesting historical note, we mention the month of publication, i.e., November, because the same authors had published another article (pp. 341–349) on the same subject matter in the October issue of the same journal. There seems to be some confusion in the relevant literature published in English, for example, Saunders⁷ writing in the Proceedings of the Royal Society ascribed (both in the citation within the text as well as in the list of references) the November 1930 paper to Pohlhausen instead of Schmidt and Beckmann. The paper in question¹³ is written in German. On page 398 of this paper, the authors, i.e., Schmidt and Beckmann acknowledge that “Herrn E. Pohlhausen, Danzig, verdanken wir die Mitteilung, daß sich diese partiellen Differentialgleichungen in gewöhnliche transformieren, wenn man $\xi = cy/\sqrt[4]{x}$ als neue Variable einführt,” i.e., “We owe the communication to Mr. E. Pohlhausen, Danzig, that these partial differential equations transform into ordinary ones when $\xi = cy/\sqrt[4]{x}$ is introduced as a new variable.” On page 402 of

their paper, Schmidt and Beckmann further acknowledge that it was Pohlhausen who painstakingly carried out the integration of the transformed differential equations for air and the results are included in Table 4 (“Zahlentafel”) and Fig. 24 of the paper by Schmidt and Beckmann.] Another much-quoted early work on similarity theory is by Ostrach.¹⁴ Sparrow¹⁵ developed an integral analysis, and Chen *et al.*¹⁸ adopted an integro-differential approach. Research is also carried out in related fields involving natural convection on a vertical plate, for example, Refs. 19 and 20 present solutions in the presence of a nanofluid, Ref. 21 deals with non-Newtonian fluids, Refs. 21–25 discuss turbulent natural convection, Ref. 26 combines the effects of radiation with natural convection, Ref. 27 establishes the fluid dynamics of magnetohydrodynamic natural convection, and Ref. 28 discusses the thermophoretic movement of nanometre-to-micrometre-sized particles in a natural convective boundary layer on a heated vertical plate. New experimental techniques for flow visualization and measurements have been reported.^{29,30} Guha and Sengupta⁶ have presented a comprehensive analysis of the effects of the finiteness of a heated horizontal plate on the thermo-fluid-dynamics of natural convection above it. Recently, Guha and Pradhan³¹ have developed a unified integral theory for natural convection on an arbitrarily inclined plate, a limiting case applied to the vertical plate. Since a practical plate is necessarily of finite length, one aspect of the present study is complementary to Ref. 6 in extending the study of finiteness to the case of a vertical plate. Even though the research field spans over a century and is still active, the present paper, according to our knowledge, is the only work which presents detailed fluid dynamics around a finite heated vertical plate and which critically assesses the theoretical formulation that is routinely included in all textbooks on the subject.

Other than establishing the full consequence of the much-used boundary condition $u = 0$ at $x = 0$ in the theoretical analyses, the CFD solutions in the present paper are designed such that it is possible to examine separately the role of a few other assumptions of the theoretical analyses as well. For example, the similarity theory or the integral theory is based on the boundary layer equations. The validity of this assumption is quantitatively assessed here since the full Navier-Stokes equations are solved for the CFD simulations. The similarity theory is also based on the assumption that the plate is semi-infinite. The effect of finiteness is established here. The present CFD solutions are carried out carefully, the domain independence and grid independence tests being conducted afresh each time a new combination of the Grashof number and Prandtl number is simulated. For accurate solutions, the domain size must be sufficiently large so that the flow quantities properly reach their quiescent values. The computations are also carried out to a high degree of precision: the maximum scaled residual for all (continuity, momentum and energy) conservation equations is set to as low as 10^{-8} (which is much lower than what is reported in the usual CFD literature). Moreover, double-precision arithmetic is used in all computations. This precision gives confidence in the physical conclusions deduced in this paper.

It should be stated here that if one wants to construct the standard similarity theory for natural convection on a heated

vertical plate, which simplifies the physical description by providing non-dimensional velocity and temperature profiles as functions of the similarity variable, then it is necessary to use the boundary condition $u = 0$ at $x = 0$. In spite of the accomplishment of the present work, we still think that the similarity theory, as the first theoretical tool, has its definite role in textbooks. However, the limitations of the similarity theory and the consequences of the boundary condition $u = 0$ at $x = 0$ have not so far been established. Generations of textbooks have reproduced the same analysis and generations of students seem to have followed the method without introspection. The present work provides a critical understanding of the similarity theory, identifies for the first time the fluid dynamic consequences of the boundary condition $u = 0$ at $x = 0$, and thereby establishes the basis of a more appropriate theoretical analysis whose predictions agree closely with experimentally measured values of the Nusselt number.

II. MATHEMATICAL FORMULATION AND A SUMMARY OF THE SIMILARITY THEORY

A short introduction to the boundary layer equations for laminar natural convection and the formulation of the classical similarity theory for natural convection on a vertical plate are presented below for ready reference. Since a major objective of the present paper is to examine the role of various approximations, particularly the role of the assumed boundary condition $u = 0$ at $x = 0$, it is hoped that this summary would be helpful for the reader. Since several similarity solutions^{13,14} were obtained many years ago, we have recomputed the value of the Nusselt number, to a high degree of precision, as a function of Grashof and Prandtl numbers. The following summary is contextual in this respect as well.

Navier-Stokes equations expressed in a Cartesian coordinate system are the governing equations for natural convection above a vertical plate. The present study considers steady, incompressible, laminar flow. A two-dimensional analysis is conducted for which the width of the plate perpendicular to the plane of the paper is infinite. The two-dimensional governing equations are as follows:

$$\frac{\partial u}{\partial x} + \frac{\partial v}{\partial y} = 0, \quad (1)$$

$$\rho \left(u \frac{\partial u}{\partial x} + v \frac{\partial u}{\partial y} \right) = f_x - \frac{\partial P}{\partial x} + \mu \nabla^2 u, \quad (2)$$

$$\rho \left(u \frac{\partial v}{\partial x} + v \frac{\partial v}{\partial y} \right) = -\frac{\partial P}{\partial y} + \mu \nabla^2 v, \quad (3)$$

$$\rho c_p \left(u \frac{\partial T}{\partial x} + v \frac{\partial T}{\partial y} \right) = k \nabla^2 T. \quad (4)$$

Here the x -axis is taken along the vertical direction (Fig. 1). u and v denote velocities, respectively, along the x - and y -axis, P denotes the absolute pressure, and T is the absolute temperature of the fluid. ρ , μ , c_p , and k are the density, dynamic viscosity, specific heat at constant pressure, and thermal conductivity, respectively, of the fluid. Body force per unit volume in the x direction is denoted by f_x ($f_x \equiv -\rho g$) where g is the gravitational acceleration.

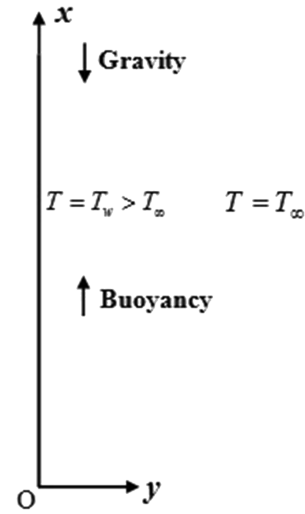


FIG. 1. A schematic for the analysis of natural convection along an isothermally heated vertical plate.

All thermophysical properties of the fluid, e.g., viscosity, specific heat, thermal conductivity, and thermal expansion coefficient, except the density, are considered to be constant. The variation of density with temperature is taken care of only in the buoyancy term of the momentum equations. In addition, the Boussinesq approximation,² which considers a linear variation of density with temperature, is adopted here. According to the Boussinesq approximation

$$\rho = \rho_\infty [1 - \beta(T - T_\infty)], \quad (5)$$

where β is the thermal expansion coefficient. β equals $1/T$ from the ideal gas approximation. T_∞ is the temperature of the quiescent fluid medium far from the heated plate and ρ_∞ is the far-field density of the quiescent fluid. Substituting the expression of ρ in the definition of f_x , we have $f_x = -\rho_\infty g [1 - \beta(T - T_\infty)]$. The viscous dissipation terms are neglected here considering the fact that the induced kinetic energy is much less than the heat transfer.³²

A. Simplified equations

With boundary layer approximations, an order of magnitude analysis reduces the y momentum equation and gives

$$\partial P / \partial y = 0. \quad (6)$$

Equation (6) suggests that P is a function of x only, and $\partial P / \partial x$ can be written as dP_∞ / dx which equals $(-\rho_\infty g)$. An order of magnitude analysis of the x -momentum equation shows that the term $\frac{\partial^2 u}{\partial x^2}$ is negligible with respect to the other terms. Along with these considerations, the variation of density with temperature is taken care of only in the buoyancy term of the momentum equations, as mentioned earlier. Therefore, the x -momentum equation can be expressed as

$$\rho_\infty \left(u \frac{\partial u}{\partial x} + v \frac{\partial u}{\partial y} \right) = \rho_\infty g \beta (T - T_\infty) + \mu \frac{\partial^2 u}{\partial y^2}. \quad (7)$$

Now, for the sake of non-dimensionalisation, a characteristic length scale L and a velocity scale u_0 are introduced.

Temperature is non-dimensionalised by $(T_w - T_\infty)$, where T_w is the constant surface temperature of the heated plate. The non-dimensionalised variables are

$$\bar{x} = \frac{x}{L}, \quad \bar{y} = \frac{y}{L}, \quad \bar{u} = \frac{u}{u_0}, \quad \bar{v} = \frac{v}{u_0}, \quad \theta = \frac{T - T_\infty}{T_w - T_\infty}, \quad (8)$$

and the simplified non-dimensionalised equations are¹

$$\frac{\partial \bar{u}}{\partial \bar{x}} + \frac{\partial \bar{v}}{\partial \bar{y}} = 0, \quad (9)$$

$$\bar{u} \frac{\partial \bar{u}}{\partial \bar{x}} + \bar{v} \frac{\partial \bar{u}}{\partial \bar{y}} = \theta + \frac{1}{\sqrt{Gr_L}} \frac{\partial^2 \bar{u}}{\partial \bar{y}^2}, \quad (10)$$

$$\bar{u} \frac{\partial \theta}{\partial \bar{x}} + \bar{v} \frac{\partial \theta}{\partial \bar{y}} = \frac{1}{\sqrt{Gr_L} Pr} \frac{\partial^2 \theta}{\partial \bar{y}^2}. \quad (11)$$

The reference velocity u_0 in Eq. (8) is chosen such that the coefficient of θ in the RHS of Eq. (10) becomes unity. This happens when $u_0 = \nu \sqrt{Gr_L}/L$, where Gr_L is the Grashof number based on the characteristic length L and is given by $Gr_L = g\beta(T_w - T_\infty)L^3/\nu^2$. Here ν is the kinematic viscosity of the fluid, defined as $\nu = \mu/\rho_\infty$. The Prandtl number of the fluid is denoted by Pr ($Pr \equiv \mu c_p/k$).

The boundary conditions are as follows:

$$\text{at } \bar{y} = 0, \quad \bar{u} = \bar{v} = 0, \quad \theta = 1, \quad (12)$$

$$\text{as } \bar{y} \rightarrow \infty, \quad \bar{u} \rightarrow 0, \quad \theta \rightarrow 0. \quad (13)$$

B. Similarity solution

Equations (9)–(11) can be transformed to a set of ordinary differential equations which give similarity solutions.² The ordinary differential equations are as follows:

$$f'''' + 3ff'' - 2f'^2 + \theta = 0, \quad (14)$$

$$\theta'' + 3Prf\theta' = 0, \quad (15)$$

In Eqs. (14) and (15), prime, double-prime, and triple-prime denote $d/d\eta$, $d^2/d\eta^2$, and $d^3/d\eta^3$, respectively. The similarity variable “ η ” is $\frac{y}{x} \left(\frac{Gr_x}{4} \right)^{\frac{1}{4}}$. f is related to the stream function $\psi(x, y)$ as follows:

$$\psi = f(\eta) \left[4\nu \left(\frac{Gr_x}{4} \right)^{\frac{1}{4}} \right]. \quad (16)$$

The boundary conditions required to solve Eqs. (14) and (15) are given as follows:

$$\text{at } \eta = 0, \quad f = f' = 0, \quad \theta = 1, \quad (17)$$

$$\text{as } \eta \rightarrow \infty, \quad f' \rightarrow 0, \quad \theta \rightarrow 0. \quad (18)$$

Numerical solutions of Eqs. (14) and (15) give the variations of f and θ as functions of η , from which the velocity and temperature fields (in terms of dimensional variables) can be constructed. The value of the local Nusselt number Nu_x ($Nu_x \equiv hx/k$) obtained from the similarity theory is given by

$$\begin{aligned} Nu_x &= - \left(\frac{Gr_x}{4} \right)^{\frac{1}{4}} \left(\frac{d\theta}{d\eta} \right)_{\eta=0} \\ &= \left(\frac{Gr_x}{4} \right)^{\frac{1}{4}} g(Pr). \end{aligned} \quad (19)$$

A study of Eqs. (14) and (15) shows that the value of $-\theta'(0) = -(d\theta/d\eta)_{\eta=0}$ depends only on Pr . This is why this functional dependence is denoted by $g(Pr)$ in Eq. (19). The function $g(Pr)$ is determined numerically as a part of the similarity solution. The average Nusselt number \overline{Nu} can be evaluated from Eq. (19) as follows:

$$\overline{Nu} \equiv \frac{\bar{h}L}{k} = \frac{1}{k} \int_0^L h dx = \frac{4}{3} \left(\frac{Gr_L}{4} \right)^{\frac{1}{4}} g(Pr). \quad (20)$$

Here, h is the local convective heat transfer coefficient and \bar{h} is the average convective heat transfer coefficient. Since the results of similarity analyses given in Ref. 14 were obtained many years ago, we recomputed these values taking advantage of modern computers with large computational resource and double-precision operations.³³ Equations (14) and (15) are solved with the boundary conditions given by Eqs. (17) and (18) by the shooting method. In this method, the system of Eqs. (14) and (15) is first reduced to a system of five first order equations. The equations can now be solved by marching forward in η , if the boundary values which are not specified at $\eta = 0$ are first guessed so that the solution process can proceed. However, the boundary values computed at $\eta \rightarrow \infty$ will depend on these guessed values and, in general, will not agree with the actual prescribed conditions at $\eta \rightarrow \infty$. Since we need to guess multiple (two) values simultaneously at $\eta = 0$ for the five first order equations (with two boundary conditions prescribed at $\eta \rightarrow \infty$), the Newton method for simultaneous non-linear equations³⁴ has been used here for finding the roots of the boundary residuals (difference between the computed and specified boundary values at $\eta \rightarrow \infty$). The fourth-order Runge–Kutta method with a small step size ($\Delta\eta$) of 0.001 is chosen for the integration of differential equations. For a numerical process, a large finite number for the maximum value of η needs to be specified (replacing the mathematical condition $\eta \rightarrow \infty$). For the present computations, $\eta_{\max} = 100$ is used to ensure that all flow parameters asymptotically approach their final values. A systematic study of the effects of varying $\Delta\eta$ and η_{\max} on the computed values of the average Nusselt number is made to confirm that the present similarity solutions are determined with a high degree of precision. The computed values of the function $g(Pr)$ in Eq. (19) are shown in Table I which demonstrates that the present Runge–Kutta integration determines the value of $g(Pr)$ with at least six decimal place precision (any difference between the last two columns of Table I occurs only in the seventh decimal place).

III. RESULTS FROM A NEW INTEGRAL THEORY

A unified integral theory has been developed for laminar natural convection over surfaces with arbitrary inclination,³¹ which can also be used to determine the average Nusselt number (\overline{Nu}) for the special case of a vertical plate. One uniqueness of this approach (as compared with the previously available integral theories) is that the theory can accommodate arbitrary orders for the polynomials representing the velocity profile (order λ) and the temperature profile (order χ). A systematic optimization given in Ref. 31 shows that for an isothermal

TABLE I. Similarity solutions for the function $g(\text{Pr})$ obtained by the 4th order Runge–Kutta integration.

Pr	$g(\text{Pr})$ ($\Delta\eta = 0.01$; $\eta_{\max} = 50$)	$g(\text{Pr})$ ($\Delta\eta = 0.001$; $\eta_{\max} = 50$)	$g(\text{Pr})$ ($\Delta\eta = 0.001$; $\eta_{\max} = 100$)
0.01	0.170 708 9	0.170 151 1	0.170 151 0
0.1	0.307 415 2	0.307 125 5	0.307 125 4
0.7	0.665 409 1	0.665 230 2	0.665 230 2
1	0.789 524 2	0.789 445 2	0.789 445 2
10	1.560 731 2	1.560 574 3	1.560 574 3
50	2.284 204 3	2.283 918 2	2.283 918 1
100	2.747 011 2	2.746 654 2	2.746 654 2

vertical plate, the best compromise is obtained at $\lambda = 4$, $\chi = 2$. The analysis given in Ref. 31 then shows that the local Nusselt number can be explicitly expressed as a function of the Grashof number and the Prandtl number. The relation for $\lambda = 4$, $\chi = 2$ is as follows:

$$Nu_x = 0.467 \left(\frac{Gr_x Pr^2}{\frac{5}{9} + Pr} \right)^{\frac{1}{4}}. \quad (21)$$

The average Nusselt number for the isothermal vertical plate of length L can be calculated from

$$\overline{Nu} = 0.623 \left(\frac{Gr_L Pr^2}{\frac{5}{9} + Pr} \right)^{\frac{1}{4}}. \quad (22)$$

The analysis given in Ref. 31 shows that the local Nusselt number for a vertical plate with constant-heat-flux boundary condition, with optimized velocity and temperature profiles $\lambda = 3$, $\chi = 2$, is as follows:

$$Nu_{x,vq} = 0.616 \left(\frac{Gr_x^* Pr^2}{\frac{4}{5} + Pr} \right)^{\frac{1}{5}}. \quad (23)$$

Gr_x^* in Eq. (23) is the modified Grashof number given by $Gr_x^* = g\beta q_w x^4 / (k\nu^2)$, where q_w is the wall heat flux. The average Nusselt number for the constant-heat-flux vertical plate of length L can be calculated from

$$\overline{Nu}_{vq} = 1.027 \left(\frac{Gr_L^* Pr^2}{\frac{4}{5} + Pr} \right)^{\frac{1}{5}}. \quad (24)$$

It is demonstrated in Ref. 31 that Eqs. (21)–(24) give the Nusselt number with accuracy comparable to that of the similarity theory. The advantage of Eqs. (21)–(24) is that the Nusselt number is expressed as explicit functions of the Grashof number and Prandtl number.

The new integral theory is briefly mentioned here for the sake of completeness. A future reader will then get updated versions of all approaches on the natural convection around a heated vertical plate—similarity theory, integral theory, constrained CFD, unconstrained CFD, and experiments—in one place. This will make the current paper a comprehensive source on the subject. The predictions of the new integral theory are included in the comparison of all approaches (Sec. V), which shows that the predictions of the explicit integral formulae are quite close to the predictions of the similarity theory (which is more rigorous than integral analysis but does not give closed-form analytical results) and exhibit the same trend in the entire

range of computations $10^4 \leq Gr_L \leq 10^8$, $0.01 \leq \text{Pr} \leq 100$. Next we turn our attention to the main theme of the present paper—CFD simulations.

IV. COMPUTATIONAL FLUID DYNAMICS SIMULATIONS

The full incompressible Navier-Stokes equations for steady, laminar natural convective flow are solved using a commercially available CFD software Fluent,³⁵ which uses the finite volume method. The dimension of the plate in the z-direction (i.e., perpendicular to the plane shown in Fig. 1) is considered to be infinitely large. Accordingly, 2-D simulations are performed utilizing double precision arithmetic. An implicit³⁶ formulation is used to solve the system of equations. The solver uses a time-marching technique^{37,38} to achieve a steady state solution as the limiting process of an unsteady simulation. All thermophysical properties are assumed constant except the density in the buoyancy term, which is modeled by the Boussinesq approximation. The second order upwind scheme provided in Fluent is used for the discretisation of the advection terms, while the central difference scheme is used for discretising the diffusion terms in both momentum and energy equations. The second order scheme is employed for pressure-discretisation. The SIMPLE algorithm is used for pressure-velocity coupling. Under relaxation factors for momentum, energy, pressure, density, and body forces are chosen, respectively, as 0.7, 1, 0.3, 1, and 1, respectively. The values are chosen such that numerical instabilities are avoided but computational time does not increase excessively.

A. Geometry and physical properties

A vertical plate of length L and thickness t_p is considered in the present study. One side of the plate (AB in Fig. 2) is maintained at a constant temperature T_w ($> T_\infty$), while the other three sides are insulated. (Of course we could maintain both the left and right sides of the plate at the same constant temperature. The buoyant jet will then be symmetric. With the prescribed asymmetric boundary conditions, we have tried to simultaneously achieve a new exploration on the evolution of an asymmetric buoyant jet.) All the four sides of the plate are subjected to no-slip condition. The plate is located exactly at the middle of the rectangular computational domain (Fig. 2), and the boundaries of this computational domain are modeled by the “pressure outlet” option available in Fluent.³⁵ The Fluent manual does not provide much detail on the actual

Since our objective is to obtain CFD results for natural convection with such high degree of accuracy that these results can be included in future textbooks as a reliable source of data, we have taken a double-ensuring strategy for selecting the all-important size of the computational domain. At first, with several initial simulations with various sizes of the adopted domain, we have *approximately* determined the required size of the domain such that various flow parameters asymptotically reach their final values at the domain boundary. We denote this domain as the region of interest (ROI). The rectangle WXYZ, shown in Fig. 2, represents the region of interest (ROI). We then adopt a much larger size of the domain for the actual simulations from which we extract the final results (such as the value of \overline{Nu}). Figure 2 shows that the boundaries of the final computational domain are l_a and l_b distances away, respectively, from the vertical and horizontal boundaries of the ROI. The difference between the initial set of simulations to determine the ROI and the final set of simulations to determine the final computational domain is that, for the latter, the boundary conditions are applied much further away (at the boundaries of the full domain) from the boundaries of the ROI where the asymptotic convergence of the various parameters is ensured. In this way, the effect of any imperfection in the application of the “pressure outlet” boundary condition is eliminated from the region of interest.

The procedure is illustrated here for a particular combination of Grashof and Prandtl numbers, viz., $Gr_L = 10^6$ and $Pr = 0.7$. From the first set of initial simulations mentioned above, it is determined that the size of the ROI in this case is a rectangle of 1.7 m height and 12.8 m width. Now, a systematic domain independence test is carried out in which the values of l_a and l_b are progressively increased and the values of important parameters at the boundaries of the ROI are monitored. Table II shows some sample results of the domain independence test for five representative domains, viz., D1, D2, . . . , D5. The mass flow rates through the four boundaries of the ROI (WX, YX, ZY, and ZW), denoted as \dot{m}_{WX} , \dot{m}_{YX} , \dot{m}_{ZY} , and \dot{m}_{ZW} , are tabulated for each of the domains. It is observed that as the domain size is changed from D4 to D5, none of the mass flow rates change up to the sixth decimal place.

In a similar manner, the sizes of the ROI and full computational domain are determined for all other combinations of Grashof and Prandtl numbers. It is found that the widths of the ROI and full computational domain mentioned above remain adequate, whereas the height of the ROI needs to be increased to 3.3 m for low values of the Prandtl number. Accordingly the

standard sizes chosen for all computations reported in Sec. V are as follows: a rectangular area of 3.3 m height and 12.8 m width ROI and a rectangular area of 6.5 m height and 25.6 m width for the full computational domain. It is recalled that the length of the plate (L) taken here is 0.1 m. This means that the computational domain is of the size $65L \times 256L$, i.e., nearly true infinity conditions have been attempted to be implemented.

C. Grid independence test

A systematic grid independence study has been carried out for many combinations of Gr_L and Pr . Four grid structures are constructed—viz., “coarse,” “medium,” “fine,” and “superfine”—as shown in Table III. The size (in the y -direction) of the first computational cell adjacent to the solid plate, Δy_1 , is a critical parameter for accurately capturing the gradients of flow variables at the surface, and hence this value is also shown in Table III. The value of Δy_1 is progressively halved as the grid is progressively refined from “coarse” to “superfine.” A non-uniform grid distribution is used in the y -direction so that the natural convective boundary layer is appropriately resolved, and at the same time, a large computational domain can be utilized so that the boundary conditions for the natural convective flow can be applied appropriately. The grid size in the y -direction is progressively increased (as one moves away from the solid surface) in geometric progression (with a ratio of 1.02 between successive grid sizes) and a limiter is placed so that a computational cell cannot become larger than 25 mm. When this limiting value is reached, a uniform grid of 25 mm is continued up to the boundary of the computational domain. The size of all grids in the y -direction in regions S4 and S8 (see Fig. 2) is uniformly Δy_1 , i.e., a very fine grid is used with a view to capture the details of the evolution of the buoyant jet. Similarly, a non-uniform grid distribution is used in the x -direction, with a geometric progression ratio of 1.02, to capture the effects of the plate edges. The grids are coarser towards the boundary of the computational domain and also towards the middle of the plate while those are finer towards the edges of the plate. In the x -direction also, a limiter of 25 mm is placed on the size of a computational cell. When the size of 25 mm is reached, geometric progression is not used any further, instead a uniform grid of 25 mm is used.

A systematic grid independence test is applied and examined for domain D5 at 25 combinations of Grashof and Prandtl numbers of which the results for five such combinations are included in the upper part of Table III as representative samples. The representative five cases are carefully selected to cover the entire range of $Gr_L \times Pr$ used for the computations. It is found that as the grid size is systematically refined (following the method described above) from “coarse” to “superfine,” the values of the computed average Nusselt number \overline{Nu} uniformly converge. Between the “fine” and “superfine” grid structures, there is no difference in \overline{Nu} up to the third decimal place at all combinations of the Grashof number and Prandtl number tested within the ranges $10^4 \leq Gr_L \leq 10^8$ and $0.01 \leq Pr \leq 100$. The data in Table III show that the relative difference in \overline{Nu} between the “fine” and “superfine” grids is of the order 10^{-6} .

Since the domain independence test described in Sec. IV B was carried out with a particular grid, a second series of grid

TABLE II. Result of the domain independence test for five computational domains ($Gr_L = 10^6$, $Pr = 0.7$).

Name of the computational domain	l_a/L	l_b/L	Mass flow rates (kg/s)			
			\dot{m}_{WX}	\dot{m}_{YX}	\dot{m}_{YZ}	\dot{m}_{ZW}
D1	0.5	4	0.000 084	0.003 126	0.000 043	0.002 617
D2	1	8	0.000 089	0.003 428	0.000 070	0.003 013
D3	2	16	0.000 094	0.003 515	0.000 088	0.003 319
D4	4	32	0.000 096	0.003 664	0.000 095	0.003 467
D5	8	64	0.000 096	0.003 664	0.000 095	0.003 467

TABLE III. Grid independence test for unconstrained flow.

For domain D5								
Grid distribution	First grid size (adjacent to the plate) (m)	No. of points in x -direction	No. of points in y -direction	\overline{Nu} $Gr_L = 10^4$ Pr = 0.01	\overline{Nu} $Gr_L = 10^5$ Pr = 0.1	\overline{Nu} $Gr_L = 10^6$ Pr = 0.7	\overline{Nu} $Gr_L = 10^7$ Pr = 10	\overline{Nu} $Gr_L = 10^8$ Pr = 100
Coarse	0.000 1	184	415	1.684 98	5.116 21	15.726 82	52.288 27	162.198 39
Medium	0.000 05	296	804	1.787 01	5.210 02	15.749 21	52.321 64	162.210 21
Fine	0.000 025	518	1472	1.795 11	5.214 21	15.750 15	52.324 03	162.214 37
Superfine	0.000 012 5	949	2515	1.795 12	5.214 23	15.750 26	52.324 35	162.214 63

For $Gr_L = 10^6$ and Pr = 0.7				
Domain	\overline{Nu} coarse grid (184 × 415)	\overline{Nu} medium grid (296 × 804)	\overline{Nu} fine grid (518 × 1472)	\overline{Nu} superfine grid (949 × 2515)
D3	15.708 73	15.732 35	15.736 73	15.736 94
D4	15.726 25	15.749 03	15.750 01	15.750 15
D5	15.726 82	15.749 21	15.750 15	15.750 26

independence tests is performed for various domains to check whether there are any finer issues involved. The results for $Gr_L = 10^6$ and Pr = 0.7 are given in the lower part of Table III. It is found that the results uniformly converge as one moves to the right along any particular row or toward the bottom of a particular column. The present CFD solutions thus compute the Nusselt number accurately at least up to the third decimal point when the domain D5 and the superfine grid structure are used.

D. Convergence criteria

Convergence criteria indicate the level of accuracy of the results obtained by a CFD simulation. In the present CFD study, we adopt a systematic procedure to determine the appropriate convergence criteria. For a specific set of geometry, boundary conditions, and thermo-physical properties, the CFD simulation is carried out up to various convergence levels. This procedure has been followed for all of the combinations of Gr_L and Pr studied here; it is seen that when the “maximum scaled residual” is changed from 10^{-7} to 10^{-8} for the “superfine grid,” any change in the average Nusselt number (\overline{Nu}) happens after the fifth decimal place. Computed values of \overline{Nu} with “maximum scaled residual” at 10^{-8} are reported in Sec. V of this paper.

E. Two sets of CFD simulations

CFD simulations are run for various combinations of the Grashof number ($10^4 \leq Gr_L \leq 10^8$) and Prandtl number ($0.01 \leq Pr \leq 100$). For each combination of Gr_L and Pr, CFD simulations are run with two alternative boundary conditions—one with constrained velocity at $x = 0$ to mimic the similarity analysis and the other with no such constraints simulating the case of a heated vertical plate in an infinite expanse of the quiescent fluid medium. The domain independence, grid independence, and convergence criteria for the CFD solution with constrained velocity at $x = 0$ are similar to those for unconstrained flow discussed in Secs. IV B–IV D, respectively,

the difference being in the domain size of the two cases, the location of the lower boundary, and the boundary condition applied there. The vertical plate is situated exactly at the centre of the computational domain for simulations with unconstrained flow. For simulations with constrained flow, the lower edge of the computational domain is flush with the lower edge of the vertical plate, i.e., the sub-domains named as S_3 , S_4 , and S_5 in Fig. 2 are absent. The boundary condition $u = 0$ is numerically implemented along the lower edge of the computational domain to mimic the similarity analysis which assumes $u = 0$ at $x = 0$. The systematic grid independence test is applied again at 17 combinations of Grashof and Prandtl numbers, and the same level of convergence up to second and third decimal places of the computed \overline{Nu} is obtained as discussed in Secs. IV C and IV D.

It can therefore be concluded that following the systematic domain independence and grid independence tests and applying a stringent convergence criterion, we have been able to determine the values of \overline{Nu} with a very high degree of precision for both constrained and unconstrained flows. With the domain “D5,” “superfine grid (949 × 2515),” and maximum scaled residual at 10^{-8} , we have been able to determine \overline{Nu} with at least five decimal place precision.

V. RESULTS AND DISCUSSION

CFD simulations are run for various combinations of the Grashof number ($10^4 \leq Gr_L \leq 10^8$) and Prandtl number ($0.01 \leq Pr \leq 100$) for a thorough understanding of the thermo-fluid-dynamics of natural convection on a heated vertical plate. Comparisons are made with the corresponding similarity solutions. For streamlining the discussion, the results are divided into a few subsections.

A. Streamline pattern and contours of flow variables

Before embarking upon a detailed quantitative analysis, we present a few theoretical and computational flow visualization results that powerfully establish a qualitative

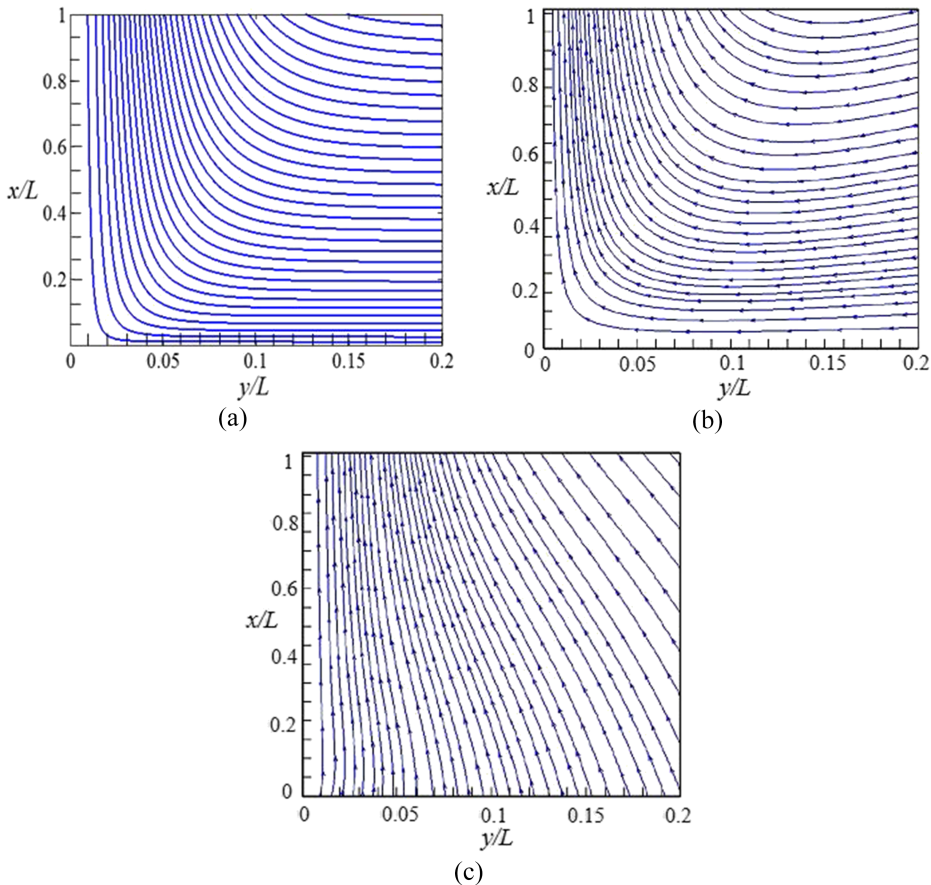


FIG. 3. (a) Streamline pattern obtained from the standard similarity theory (for $Gr_L = 10^6$ and $Pr = 0.7$). (b) Streamline pattern obtained from the present CFD simulation with constrained flow (for $Gr_L = 10^6$ and $Pr = 0.7$). (c) Streamline pattern obtained from the present CFD simulation with unconstrained flow (for $Gr_L = 10^6$ and $Pr = 0.7$).

understanding of the physical situation. Figure 3(a) shows the streamline pattern corresponding to the standard similarity theory. It is recalled that all similarity analyses^{1–5} assume the boundary condition $u = 0$ at $x = 0$. Figure 3(b) shows the streamline pattern which is obtained by post-processing CFD solutions (of the Navier-Stokes equations) with constrained velocity ($u = 0$) at $x = 0$ to mimic the similarity analysis. Figure 3(c) shows the streamline pattern which is obtained by post-processing CFD solutions with no such constraints on the u -velocity at $x = 0$, simulating the case of a heated vertical plate in an infinite expanse of the quiescent fluid medium. Figures 3(a)–3(c) are drawn to the same scale, the computations being at the same Grashof and Prandtl numbers ($Gr_L = 10^6$ and $Pr = 0.7$). The change in the stream function between any two consecutive streamlines of Figs. 3(a)–3(c) is exactly the same (which is, to be precise, $3.3 \times 10^{-5} \text{ m}^3/\text{s}$ per unit depth) so that direct comparisons are possible.

Although the principle of constructing streamlines is rather straightforward, the present authors have not come across an equivalent of Fig. 3(a) anywhere in the literature or even a discussion on what streamline pattern would be the consequence of the assumptions made for developing the similarity analysis. A comparison of Figs. 3(a) and 3(c) provides a stunning display of the differences in the fluid dynamics of entrainment. Whereas the detailed computation establishes that most of the entrained fluid (over 90% as established later in Sec. V B) comes from the bottom of the domain when a heated plate is placed in a large expanse of the fluid, the similarity theory compels all (100%) of the fluid to be sucked

from the side. One important utility of the additional set of computations displayed in Fig. 3(b) is that we have been able to reproduce the streamline pattern of the similarity theory by CFD simulations. Since the only difference between the two sets of CFD simulations lies in the boundary condition imposed on the u -velocity at $x = 0$, we conclude that the totally different streamline pattern at the bottom and side boundaries of the computational domain are the result of the assumption of the boundary condition $u = 0$ at $x = 0$ used in the similarity theory.

A comparison of Figs. 3(a)–3(c) at the top boundary shows that there is no fluid entrainment from the top side in the similarity theory, but there is a similar level (small but finite) of downward movement of the fluid through the right side of the top boundary in both sets of CFD simulations. This establishes the conclusion that fluid entrainment through the top boundary is the result of the finite extent of the heated plate in the CFD simulations (the similarity theory assumes that the plate is semi-infinite).

Figures 4 and 5 show, respectively, the velocity and temperature contours obtained by the CFD simulations with unconstrained u -velocity. The right side of the plate is at a raised but uniform temperature (isothermally heated). The other three sides of the plate are insulated. The flow field and the temperature field on the left and right sides of the plate are not the same (left-right asymmetry). The main natural convective boundary layer forms on the right side; however, Fig. 4 shows that there is a small movement of the fluid on the left side of the plate as well, as a small fraction of the entrained fluid at the leading edge of the plate spills over to the left side.

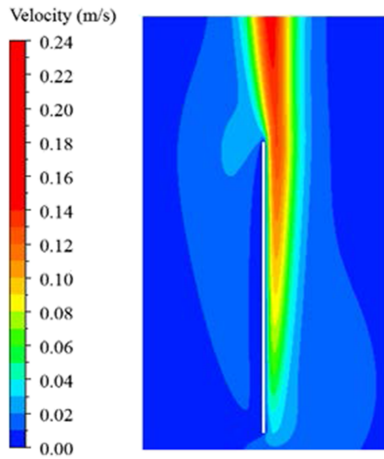


FIG. 4. Velocity contours adjacent to a heated vertical plate subjected to a constant wall temperature. (Predictions of the present CFD simulations with unconstrained flow for $Pr = 0.7$ and $Gr_L = 10^6$ with $T_w - T_\infty = 25$ K.)

As the buoyant jet leaves the trailing edge of the plate, it bends over the plate (see Fig. 4) due to the left-right asymmetry and due to the finite thickness of the plate.

As the jet leaves the plate, more and more fluid can be entrained from the left side as well. Consequently, as the vertical distance above the plate increases, there is a tendency for the centreline of the jet to align with the midplane of the plate and for the velocity of entrainment at the left and that at the right to equilibrate. This evolution of jet asymmetry is quantitatively described later in Sec. V C.

From the temperature contour in Fig. 5, it can be seen that the maximum temperature of the fluid occurs close to the plate. The maximum value of the temperature inside the free jet occurs around the centreline of the jet but its magnitude decreases as the vertical distance above the plate increases. The velocity along the centreline of the buoyant jet, in contrast, tends to increase as the vertical distance increases (see Fig. 4), as a consequence of buoyancy and the continued entrainment of the surrounding fluid.

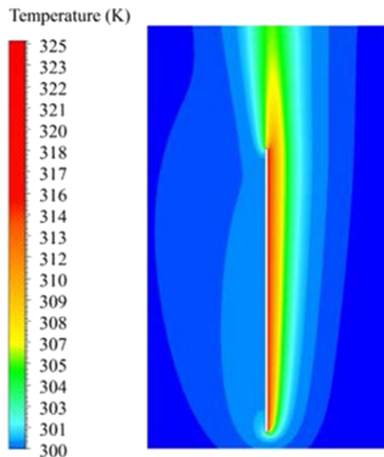


FIG. 5. Temperature contours adjacent to a heated vertical plate subjected to a constant wall temperature. (Predictions of the present CFD simulations with unconstrained flow for $Pr = 0.7$ and $Gr_L = 10^6$ with $T_w - T_\infty = 25$ K.)

B. Behaviour of directional mass fluxes

At the trailing edge of a finite heated vertical plate, a jet of fluid containing heated air emanates from the flow domain. This outgoing mass flow rate (per unit depth) at this exit plane (i.e., at the horizontal plane flush with the trailing edge of the plate) is denoted by \dot{m}_{out} . This mass flux is replenished by the flow of air through the three planes AD, DC, and EC of a rectangle ABCD, which is constructed with side AB coincident with the heated side of the plate. The location of the side CD is variable. The physical configuration can be appreciated from Fig. 2. The relative proportions of the mass fluxes that get entrained from the three sides are important indicators of the underlying fluid mechanics that determine the natural convective heat transfer. It is shown below that the relative proportions are widely different between the predictions of the similarity theory and constrained CFD and unconstrained CFD simulations.

In the proximity to the plate, the velocity of the fluid on the line BC is upward (the x component of velocity is positive) due to the buoyant jet. Farther from the plate, the velocity of the fluid on the line BC is downward (the x component of velocity is negative). So there is a point on the line BC where the x component of velocity is zero. This important point on the side BC is denoted by E. So the buoyant jet emerges fully through side BE and the fluid enters the control volume ABCD through edges AD, DC, and EC. For the inflows, let us denote the mass flow rates through AD, DC, and EC by $(\dot{m}_{in})_{bottom}$, $(\dot{m}_{in})_{side}$, and $(\dot{m}_{in})_{top}$, respectively. The three inflow rates are non-dimensionalized by the outflow rate \dot{m}_{out} , the non-dimensional quantities being denoted by a hat ($\hat{\cdot}$). So, $(\hat{m}_{in})_{bottom} \equiv (\dot{m}_{in})_{bottom}/\dot{m}_{out}$, and so on. Now these non-dimensional mass flow rates depend on the position of the side DC. In this study, the position of DC has been systematically shifted away from the plate, and for each new position of DC, the three non-dimensional mass flow rates are determined. This is done until each of $(\hat{m}_{in})_{bottom}$, $(\hat{m}_{in})_{side}$, and $(\hat{m}_{in})_{top}$ plateaus to their respective limiting values, i.e., they become independent of the position of DC. An example of obtaining these limiting ratios at $Gr_L = 10^6$ and $Pr = 0.7$ is shown in Table IV. This painstaking process is repeated at every other combination of Gr_L and Pr reported in this paper. Two representative variations of $(\hat{m}_{in})_{bottom}$ with Gr_L and Pr are shown in Fig. 6.

From Table IV, Fig. 6, and other computations not graphically displayed here, the following general observations can be made. (i) Table IV shows that as the value of l_c/L increases, i.e., the plane DC is shifted farther from the heated plate,

TABLE IV. Change of $(\hat{m}_{in})_{bottom}$, $(\hat{m}_{in})_{side}$, and $(\hat{m}_{in})_{top}$ with varying distance of CD from AB for $Gr_L = 10^6$ and $Pr = 0.7$.

l_c/L	$(\hat{m}_{in})_{bottom}$	$(\hat{m}_{in})_{side}$	$(\hat{m}_{in})_{top}$
8	0.9544	0.0416	0.0040
12	0.9689	0.0170	0.0141
16	0.9729	0.0071	0.0200
32	0.9736	0.0037	0.0227
64	0.9737	0.0036	0.0227

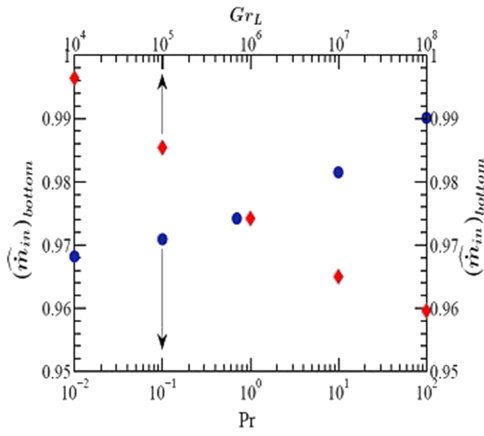


FIG. 6. Variation of mass flow fraction entrained from the bottom $(\hat{m}_{in})_{bottom}$ with Gr_L (for $Pr = 0.7$) and with Pr (at $Gr_L = 10^6$).

the values of $(\hat{m}_{in})_{bottom}$, and $(\hat{m}_{in})_{top}$ increase and the value of $(\hat{m}_{in})_{side}$ decreases. (ii) There is little change in the three non-dimensional mass fluxes as the value of l_c/L is increased from 32 to 64, indicating that the mass fluxes have nearly attained their respective limiting values. (iii) Figure 6 shows that the limiting value of $(\hat{m}_{in})_{bottom}$ decreases slightly as Gr_L is changed by four orders of magnitude and increases slightly as Pr is changed by four orders of magnitude. (iv) There is a small but finite value of $(\hat{m}_{in})_{top}$; this entrainment flow is the result of the heated plate being finite in extent. In the similarity or integral theory,¹⁻⁵ $(\hat{m}_{in})_{top}$ is found to be exactly zero since the plate is assumed semi-infinite. (v) In the similarity theory,¹⁻⁵ 100% of the entrainment flow comes through the side (plane CD in Fig. 2), and no fluid entrainment takes place from the bottom (because of the boundary condition $u = 0$ at $x = 0$) or from the top (because of the assumption of semi-infinite extent of the plate). In contrast, the present CFD simulations with unconstrained flow show that the majority of the flow entrainment (more than 90%) takes place from the bottom (plane AD in Fig. 2). The smallest fraction of entrainment takes place from the side. [However, it should be noted that $(\hat{m}_{in})_{side}$ does not go to zero as l_c/L is increased, but it assumes a small finite value.] The physics of actual entrainment is thus very different from what can be constructed from the predictions of the standard similarity theory.

C. Evolution of the asymmetry of the buoyant jet

The asymmetry of the buoyant jet could be visualized from the contour plots in Figs. 4 and 5. The asymmetry arises for two reasons: (i) different boundary conditions being applied on the two sides of the plate and (ii) a finite thickness being assigned to the plate. The physics of the evolution of the asymmetry is studied here. As far as we know, this topic has not been investigated previously. The asymmetry is reflected both in the profiles of u -velocity (representing the vertical velocity in the jet) and v -velocity (which determines the mass flow rate of entrainment from the two sides of the jet). Both topics are discussed below.

The physical configuration is displayed in Fig. 2. It is to be realized that even though the left side of the plate is insulated, a small portion of the entrained fluid at the leading

(bottom) edge of the plate spills over to the left side and there is a (small) natural convective motion on the left side of the plate as well. Similar to the point E on the top-right side of the plate, there is also a point of zero vertical velocity to the left of the plate. This is denoted by E' . For the case $Gr_L = 10^6$ and $Pr = 0.7$, the present computations show that $BE \approx 1.145 L$ and $B'E' \approx 1.247 L$. A floating plane $G^i F^i$, at a distance l_d above the trailing edge of the plate, is constructed to complete a rectangular control volume $E' G^i F^i E$ (Fig. 2). For convenience, the superscript i (denoting the locations of the points F^i and G^i) are such that $EF^i = E'G^i = i \times \overline{AB} = i \times L$ for $i = 1/2, 1, 2, 4, 8$. The superscript i thus directly indicates the non-dimensional vertical distance of the plane $G^i F^i$ above the trailing edge of the plate. As a result of different boundary conditions on the two sides of the plate, the magnitude of the v -velocity, and hence the mass flow rate per unit depth, along EF^i and along $E'G^i$ are different from each other. The mass flow rate through $E'G^i$ is denoted by \dot{m}_{left}^i and that through EF^i is denoted by \dot{m}_{right}^i . The ratio of \dot{m}_{left}^i and \dot{m}_{right}^i is denoted by r^i . Hence,

$$r^i = \frac{\dot{m}_{left}^i}{\dot{m}_{right}^i}. \quad (25)$$

The mass flow rate ratio r^i is plotted against Gr_L and Pr in Figs. 7 and 8, respectively, for the chosen five values of i . It shows that farther from the plate (i.e., with increasing value of i) the asymmetry in mass flow entrainment decreases and the ratio r^i tends to unity. It is also seen that the asymmetry between the mass flow rate through EF^i and $E'G^i$ decreases more rapidly with increasing values of Gr_L and decreasing values of Pr . This can be attributed to the increased role of viscosity which tends to establish symmetry.

The evolution of the asymmetry in the u -velocity is shown in Fig. 9. In order to clearly expound the physics, the velocity profiles are displayed at four values of l_d/L (viz., 0, 0.1, 0.4, and 1), all computations corresponding to $Gr_L = 10^6$ and $Pr = 0.7$. The following observations can be made. (i) At $l_d/L = 0$, i.e., even at a horizontal plane flush with the trailing edge of

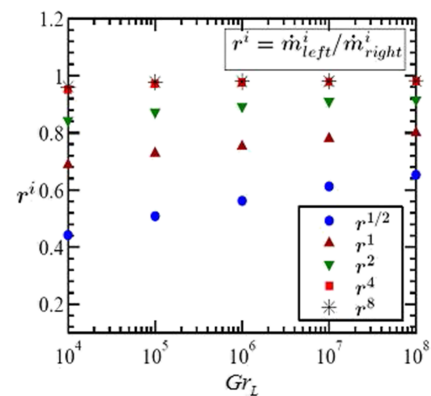


FIG. 7. Variation with Gr_L of the ratio of the rate of mass flow entrainment from the left and that from the right at different heights above the top edge of the vertical plate. [Predictions of the present CFD simulations with unconstrained flow at $Gr_L = 10^6$. The ordinate r^i represents the ratio of the left and right mass fluxes entering through a height $i \times L$ above the top edge of the vertical plate, where L is the length of the plate and five values of i are chosen ($i = 1/2, 1, 2, 4, 8$).]

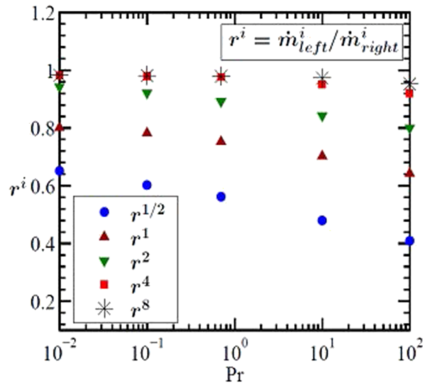


FIG. 8. Variation with Pr of the ratio of the rate of mass flow entrainment from the left and that from the right at different heights above the top edge of the vertical plate. [Predictions of the present CFD simulations with unconstrained flow at $Gr_L = 10^6$. The ordinate r^i represents the ratio of the left and right mass fluxes entering through a height $i \times L$ above the top edge of the vertical plate, where L is the length of the plate and five values of i are chosen ($i = 1/2, 1, 2, 4, 8$).]

the plate, there exists a distribution of the vertical velocity on the left (insulated) side of the plate. This is consistent with our earlier description that there exists a small natural convective current on the insulated side of the plate. (ii) As l_d/L increases, i.e., as the jet moves further above the plate, there is a tendency to restore the left-right symmetry in the u -velocity distribution. This happens mainly through adjustment in the velocity distribution on the left side; the velocity distribution on the right side changes only a little. (iii) The maximum value of the u -velocity increases with increasing l_d/L . (iv) The previous two behaviours occur over different length scales. The restoration of the left-right symmetry happens rather quickly; Fig. 9 shows that the jet becomes reasonably symmetric (the right side, though, still having a slightly greater velocity) when $l_d/L \sim 1$. The maximum u -velocity, on the other hand, is seen to increase considerably even as far as $l_d/L \sim 4$. (v) Figure 9 shows that at $l_d/L = 0$, there are two maxima, one on the left and the other on the right side. At $l_d/L = 0.1$, the profile has only maxima on the right. The transition from two-maxima to one-maxima solution is interesting and is virtually accomplished by $l_d/L \sim 0.05$. (vi) As l_d/L increases, the location of

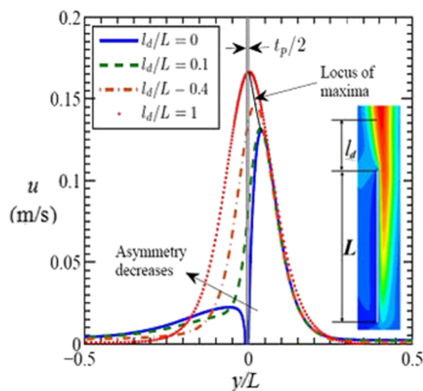


FIG. 9. Progressive development of the axial velocity profile in the buoyant jet at different heights above the top edge of the vertical plate. (Predictions of the present CFD simulations with unconstrained flow for $Pr = 0.7$ and $Gr_L = 10^6$ with $T_w = 325$ K.)

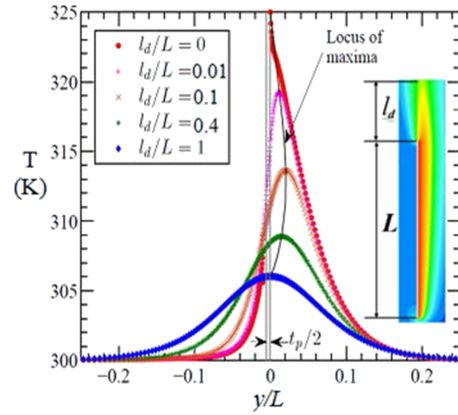


FIG. 10. Progressive development of the temperature profile in the buoyant jet at different heights above the top edge of the vertical plate. (Predictions of the present CFD simulations with unconstrained flow for $Pr = 0.7$ and $Gr_L = 10^6$ with $T_w = 325$ K. The maximum decreases as l_d/L increases.)

the maximum u -velocity shifts toward the left, tending toward the vertical line drawn through the middle of the plate. (vii) Figure 10, which displays the evolution of the temperature profile, shows the process of equilibration of temperature as l_d/L increases. At $l_d/L = 0$, the temperature profile is most asymmetric with a step change at $y = 0$. As l_d/L increases, the location of the maxima in temperature moves at first to the right (i.e., toward the heated side of the plate) and then to the left. Like the profile of the axial velocity (shown in Fig. 9), the temperature profile (Fig. 10) also becomes nearly symmetric at $l_d/L \sim 1$, although the jet still remains buoyant, and the evolution of temperature and axial velocity continues up to much larger values of l_d/L .

The above discussion establishes a qualitative and quantitative description of the evolution of the asymmetry in the buoyant jet. It is shown that at large values of l_d/L , the buoyant jet tends to be symmetric with respect to an axis that passes through the vertical mid-plane of the plate. An interesting interpretation of this phenomenon is that, sufficiently above the plate, the jet tends to lose its history of origination.

D. Variation of the computed Nusselt number

The variations in the local Nusselt number Nu_x and the average value of the Nusselt number \bar{Nu} (averaged over the finite length of the plate) are computed and compared in this section. CFD simulations are run for various combinations of the Grashof number ($10^4 \leq Gr_L \leq 10^8$) and Prandtl number ($0.01 \leq Pr \leq 100$). For each combination of Gr_L and Pr , CFD simulations are run with two alternative boundary conditions—one with constrained velocity at $x = 0$ to mimic the similarity analysis and the other with no such constraints simulating the case of a heated vertical plate in an infinite expanse of the quiescent fluid medium. Table V shows a summary comparison of the results of CFD simulations, similarity analyses, and experiments. (The combination of $Gr_L = 10^4$ and $Pr = 0.01$ may stretch the applicability of the boundary layer analysis, and the combination of $Gr_L = 10^8$ and $Pr = 100$ may stretch the applicability of the laminar flow analysis. Nevertheless, we have kept these limiting combinations in Table V and found that similar trends continue at these values,

TABLE V. Comparison of the Nusselt number obtained by the present CFD simulations, similarity theory, and experiment.

Variation with the Prandtl number (at $Gr_L = 10^6$)						
Pr	\overline{Nu} (similarity recomputed) Eq. (20)	\overline{Nu} (integral ³¹) Eq. (22)	\overline{Nu} (CFD with constrained flow)	\overline{Nu} (CFD with unconstrained flow)	\overline{Nu} (experimental)	
0.01	3.805	3.671	3.880	4.988	5.5 ¹¹	
0.1	6.872	6.920	6.984	8.424	9.2 ¹¹	
0.7	14.875	15.563	15.108	15.750	16.0 ¹¹	
10	34.891	34.545	35.405	29.784	30.5 ⁹	
100	61.417	62.180	62.216	50.888	51.5 ⁹	
Variation with the Grashof number (at Pr = 0.7)						
Gr_L	\overline{Nu} (similarity recomputed) Eq. (20)	\overline{Nu} (integral ³¹) Eq. (22)	\overline{Nu} (CFD with constrained flow)	\overline{Nu} (CFD with unconstrained flow)	\overline{Nu} (experimental)	
10^4	4.704	4.922	4.958	5.826	5.4 ¹¹	
10^5	8.365	8.752	8.646	9.358	9.1 ¹¹	
10^6	14.875	15.563	15.108	15.750	16.0 ¹¹	
10^7	26.453	26.676	26.615	27.207	28 ⁹	
10^8	47.041	49.215	47.226	47.762	48 ⁹	
At various combinations of Grashof and Prandtl numbers						
Gr_L	Pr	\overline{Nu} (similarity recomputed) Eq. (20)	\overline{Nu} (integral ³¹) Eq. (22)	\overline{Nu} (CFD with constrained flow)	\overline{Nu} (CFD with unconstrained flow)	\overline{Nu} (experimental)
10^4	0.01	1.202	1.215	1.203	1.795	1.8 ¹¹
10^4	0.1	2.173	2.188	2.175	2.988	3.1 ¹¹
10^4	10	11.034	10.924	11.516	9.184	9.2 ¹¹
10^4	100	19.422	19.663	20.209	16.849	17 ¹¹
10^5	0.01	2.137	2.161	2.015	2.984	3.1 ¹¹
10^5	0.1	3.864	3.891	3.816	5.214	5.5 ¹¹
10^5	10	19.621	19.426	19.816	16.521	17 ¹¹
10^5	100	34.520	34.967	35.115	29.614	30.5 ⁹
10^7	0.01	6.759	6.832	6.329	9.416	9.2 ¹¹
10^7	0.1	12.220	12.306	11.928	17.484	17 ¹¹
10^7	10	62.046	61.431	63.218	52.324	51.5 ⁹
10^7	100	109.215	110.574	112.214	98.310	97 ⁹
10^8	0.01	12.015	12.148	12.995	16.416	17 ¹¹
10^8	0.1	21.731	21.883	22.224	29.292	30.5 ⁹
10^8	10	110.335	109.241	107.824	98.214	97 ⁹
10^8	100	194.219	196.632	191.926	162.215	160 ⁹

including the fact that the Nusselt numbers determined from the unconstrained CFD simulations are still close to the experimentally measured ones.) The experimental values of \overline{Nu} given in Table V have been extracted from Refs. 9 and 11. Reference 11 reports the measurement at low Grashof numbers (values not covered in Ref. 9); unfortunately, the issue of experimental errors is not mentioned there, although the paper seems to be well respected in the literature. The authors of Ref. 9 have addressed the topic of experimental errors in detail. They mention that experimental errors may arise from “accuracy of measurements, effects of aberration, end effects, and effects of conduction and radiation.” They discuss each source of error in turn and what precautions they have taken to minimise them; the final value of the experimental uncertainty is however not quantified.

Table V establishes that, in general, (i) the predictions of the similarity theory and those of CFD with constrained flow are close, (ii) the difference between the predictions of the similarity theory and those of the CFD with unconstrained flow can be large, particularly when the Prandtl number is small or large, and (iii) out of the various predictions, the experimental values of \overline{Nu} are always closest to the predictions of CFD simulations with unconstrained flow.

Both sets of CFD simulations (with and without constrained flow) solve the full Navier-Stokes equations. The demonstration in Table V that, at all combinations of Grashof and Prandtl numbers, \overline{Nu} determined by CFD with constrained flow is quite close to \overline{Nu} determined by the similarity solution establishes the conclusion that the boundary-layer approximations inherent in the similarity theory are not a major

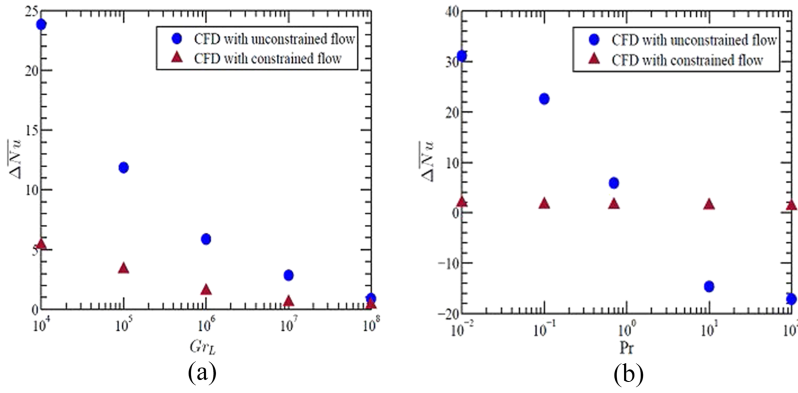


FIG. 11. (a) Variation of $\Delta \overline{Nu}$ with Gr_L (for $Pr = 0.7$). (b) Variation of $\Delta \overline{Nu}$ with Pr (at $Gr_L = 10^6$).

source of error. The difference between the two sets of CFD simulations is significant at all combinations of Grashof and Prandtl numbers. This establishes that the boundary condition $u = 0$ at $x = 0$ causes major alteration in the fluid dynamics and consequently in the computed value of \overline{Nu} , and this long-used boundary condition is therefore the principal cause for the vulnerability of the similarity analysis. Table V shows that, for certain combinations of Gr_L and Pr , the similarity theory underpredicts the value of \overline{Nu} as compared with the experiment, while for certain other combinations of Gr_L and Pr , the similarity theory overpredicts. The CFD with unconstrained velocity brings the theoretical analysis closer to experiments in both situations.

To assist the discussion, we define

$$\Delta \overline{Nu} = \frac{\overline{Nu} \text{ from CFD} - \overline{Nu} \text{ from Similarity}}{\overline{Nu} \text{ from Similarity}} \times 100. \quad (26)$$

Two sets of values of $\Delta \overline{Nu}$, corresponding to two sets of CFD simulations with and without constrained flow, are plotted in Figs. 11(a) and 11(b) to display, respectively, its variation with Gr_L and Pr . The difference between the two sets of $\Delta \overline{Nu}$ is indicative of the influence of the boundary condition $u = 0$ at $x = 0$. $\Delta \overline{Nu}$ can be significant for the CFD simulation with unconstrained flow. Figure 11(a) shows that $\Delta \overline{Nu}$ is positive, but Fig. 11(b) shows that $\Delta \overline{Nu}$ can be positive or negative. $|\Delta \overline{Nu}|$ decreases continuously with an increase in Gr_L . But in the case of variation with Pr , $|\Delta \overline{Nu}|$ is the least in the moderate range of Pr (≈ 1) and increases towards the very high or low values of Pr . A good discussion on the role of the Prandtl number in natural convection, particularly in determining the relative

thicknesses of the velocity and thermal boundary layers, is given in Ref. 41.

Other than the average Nusselt number, \overline{Nu} , giving overall heat transfer characteristics of natural convection over a heated vertical plate, the variation of the local Nusselt number Nu_x is also important to understand complementary aspects of heat transfer. It is found that at $Gr_L = 10^6$ and $Pr = 0.7$, the values of Nu_x calculated by the similarity theory, CFD with constrained flow, and CFD with unconstrained flow are almost the same in the middle portion of the vertical plate (hence not graphically illustrated), but there are differences near the leading edge [Fig. 12(a)] and the trailing edge [Fig. 12(b)]. There are subtle differences in the physics. Figure 12(a) shows that there is only a modest difference between the predictions of similarity theory and CFD with constrained flow. This difference is caused by the additional boundary layer approximations adopted in the similarity theory, which are not valid near the leading edge. There is much greater difference between the two sets of CFD predictions since the boundary condition $u = 0$ at $x = 0$ significantly alters the streamline pattern near the leading edge, altering the heat transfer there. Figure 12(b), in contrast, shows that the two sets of CFD solutions are quite close to each other, both being significantly different from the similarity analysis. This difference is caused by the assumption of semi-infiniteness in the similarity theory, whereas both CFD solutions capture the effects of finite length and finite thickness of the plate. The small difference between the two sets of CFD solutions signifies that, even at the trailing edge, there is some residual effect left of the assumed boundary condition $u = 0$ at $x = 0$ in one set of CFD simulation.

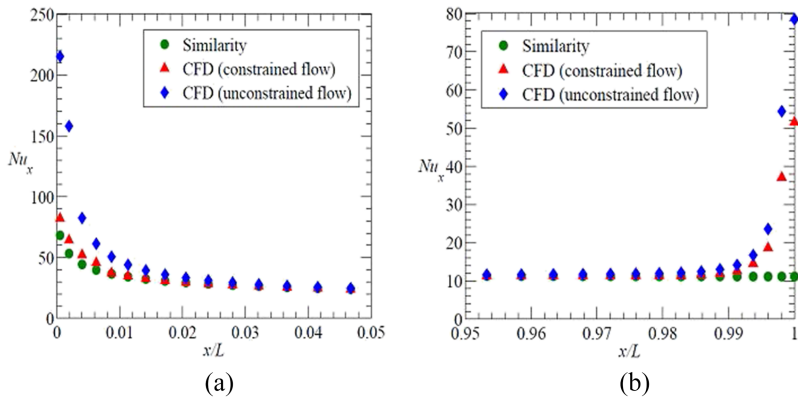


FIG. 12. (a) Variation of the local Nusselt number with the distance along the plate near the leading edge (for $Gr_L = 10^6$ and $Pr = 0.7$). (b) Variation of the local Nusselt number with the distance along the plate near the trailing edge (for $Gr_L = 10^6$ and $Pr = 0.7$).

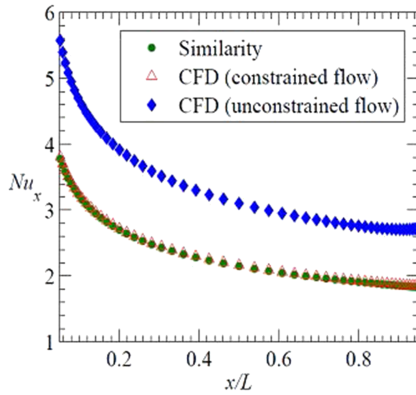


FIG. 13. Variation of the local Nusselt number with the distance along the plate in the middle portion of the plate (for $Gr_L = 10^6$ and $Pr = 0.01$).

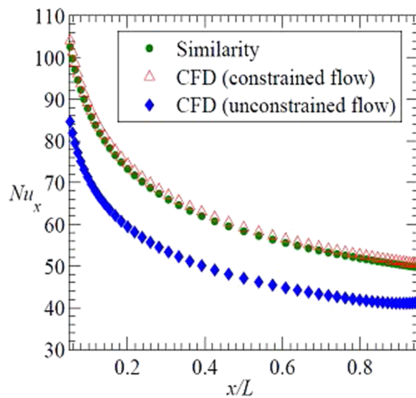


FIG. 14. Variation of the local Nusselt number with the distance along the plate in the middle portion of the plate (for $Gr_L = 10^6$ and $Pr = 100$).

It is commented that at $Gr_L = 10^6$ and $Pr = 0.7$, the values of Nu_x calculated by the similarity theory, CFD with constrained flow, and CFD with unconstrained flow are almost the same in the middle portion of the vertical plate. This is not the case when the Prandtl number is either small or large. Figures 13 and 14 display the results, respectively, for $Pr = 0.01$ and $Pr = 100$. It is found that the predictions of the similarity theory and CFD with constrained flow are almost superposed in the middle portion of the vertical plate, but the CFD solutions with unconstrained flow (which is closer to the experimental values) are significantly different. Figure 13 shows that for $Pr = 0.01$, Nu_x determined by CFD with unconstrained flow is significantly greater than that determined by the other two methods everywhere on the plate. Figure 14 shows that for $Pr = 100$, Nu_x determined by CFD with unconstrained flow is significantly smaller than that determined by the other two methods everywhere on the plate. These behaviours are reflected in the average values of the Nusselt number, \overline{Nu} , discussed previously.

VI. CONCLUSION

A compulsory element of all textbooks on natural convection has been a detailed similarity analysis for laminar natural convection on a heated semi-infinite vertical plate and a routinely used boundary condition for such analysis is $u = 0$ at

$x = 0$. The same boundary condition continues to be assumed in related theoretical analyses, even in recent publications. The present work examines the consequence of this long-held assumption, which appears to have never been questioned in the literature, on the fluid dynamics and heat transfer characteristics. The assessment has been made here by solving the Navier-Stokes equations numerically with two boundary conditions—one with constrained velocity at $x = 0$ to mimic the similarity analysis and the other with no such constraints simulating the case of a heated vertical plate in an infinite expanse of the quiescent fluid medium. It is found that the fluid flow field given by the similarity theory is drastically different from that given by the CFD simulations with unconstrained velocity. The difference is strikingly visualised by drawing, for the first time, the streamline patterns [Figs. 3(a) and 3(c)]. This also reflects on the Nusselt number (Table V), the prediction of the CFD simulations with unconstrained velocity being quite close to the experimentally measured values at all Grashof and Prandtl numbers (this is the first time theoretically computed values of \overline{Nu} are found to be so close to the experimental values). The difference of the Nusselt number ($\Delta\overline{Nu}$) predicted by the similarity theory and that by the CFD simulations with unconstrained velocity (as well as the measured values), both computed with high degree of precision, can be very significant, particularly at low Grashof numbers and at Prandtl numbers far removed from unity. Computations show that at $Pr = 0.7$, $\Delta\overline{Nu}$ increases with decreasing Gr_L reaching about 25% at $Gr_L = 10^4$. Similarly, $|\Delta\overline{Nu}|$ is the least in the moderate range of Pr (≈ 1) and increases towards the very high or low values of Pr , reaching about 31% at $Pr = 0.01$, $Gr_L = 10^6$. The maximum deviation is found for the combination of lowest Grashof and Prandtl numbers; for $Gr_L = 10^4$ and $Pr = 0.01$, $\Delta\overline{Nu}$ is about 50%. Thus, for quantitative predictions, the available theory (i.e., similarity analysis) can be rather inadequate.

Both sets of CFD simulations (with and without constrained flow) solve the full Navier-Stokes equations. The demonstration in Table V that, at all combinations of Grashof and Prandtl numbers, \overline{Nu} determined by CFD with constrained flow is quite close to \overline{Nu} determined by the similarity solution establishes the conclusion that the boundary-layer approximations inherent in the similarity theory are not a major source of error. The difference between the two sets of CFD simulations (constrained and unconstrained) is significant at all combinations of Grashof and Prandtl numbers. This establishes that the boundary condition $u = 0$ at $x = 0$ causes major alteration in the fluid dynamics and consequently in the computed value of \overline{Nu} , and this long-used boundary condition is therefore the principal cause for the vulnerability of the similarity analysis. Table V shows that for certain combinations of Gr_L and Pr , the similarity theory underpredicts the value of \overline{Nu} as compared with the experiment, while for certain other combinations of Gr_L and Pr , the similarity theory overpredicts. The CFD with unconstrained velocity brings the theoretical analysis closer to experiments in both situations.

With the help of the CFD simulations, the details of the fluid dynamics, particularly the physics of fluid entrainment, are thoroughly studied. It is shown that the relative proportions of the fluid entrainment from the bottom, top, and side of the

vertical plate depend on the size of the region of interest (ROI). As the size of the ROI is made large, most of the entrained fluid comes from the bottom, a little bit from the top and almost no fluid enters from the side; the nature of entrainment is opposite in the similarity analysis for which all the fluid enters from the side and no fluid enters either from the bottom or the top.

The CFD solutions further demonstrate the effects of finite length and finite thickness of the plate on the flow field (being complementary to a recent paper⁶) and the shape of the buoyant jet. The different boundary conditions on the two sides of the vertical plate (introduced deliberately here so that the new exploration of the evolution of an asymmetric buoyant jet is possible) and the presence of a finite thickness of the vertical plate make the buoyant jet bend over the top edge of the plate and make the evolution of entrainment from the two sides of the free buoyant jet different. The entrainment velocity from the two sides, however, equilibrates at a certain distance above the plate. The asymmetry in the velocity and temperature fields above the plate due to different thermal conditions in the two sides of the plate decreases more rapidly when Pr is smaller and Gr_L is greater. It is shown (Figs. 9 and 10) that sufficiently above the plate, the distributions of axial velocity and temperature in the buoyant jet tend to be symmetric with respect to an axis that seems to pass through the vertical mid-plane of the plate, i.e., the jet tends to lose its history of origination.

ACKNOWLEDGMENTS

The authors are grateful to Mr. Sayantan Sengupta and Mr. Kaustav Pradhan for their help.

APPENDIX: SUMMARY OF CFD SIMULATIONS FOR CONSTANT HEAT FLUX CONDITION

All results and discussion given in the main text of the paper are for an isothermal vertical plate. Several CFD simulations were run for another surface boundary condition, viz., the constant heat flux boundary condition for the sake of completeness. Such additional computations showed that although the numerical values of the various parameters such as the Nusselt number were slightly different from their isothermal counterparts, the broad physical picture of natural convective heat transfer, the physics of entrainment, and the evolution of the buoyant jet remain essentially the same. The conclusion regarding the inappropriateness of the boundary condition $u = 0$ at $x = 0$ in the similarity analysis for constant heat flux also remains valid. Hence only one test case is reported below for the sake of brevity. Figure 15 shows the computed temperature contours for an assumed constant surface heat flux of 100 W/m^2 in a fluid with $Pr = 0.7$. A comparison with Fig. 5 shows overall similarity, although there are subtle differences. As an example, it should be noted from Fig. 15 that the temperature of the solid surface is, in this case, variable (it increases with increasing x). Detailed computational tests show that when the plateau is reached (see Sec. V B), the fractions of the fluid entering from the bottom, top, and side are, respectively, 96.15%, 3.04%, and 0.81%.

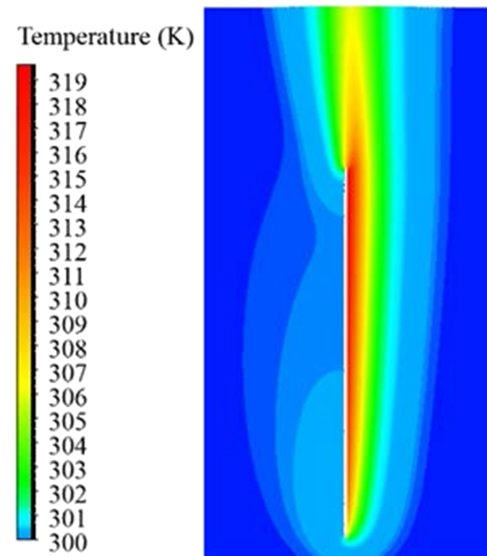


FIG. 15. Temperature contours adjacent to a heated vertical plate subjected to a constant wall heat flux. (Predictions of the present CFD simulations with unconstrained flow for $Pr = 0.7$ and $\dot{q}_w = 100 \text{ W/m}^2$.)

The similarity analysis gives $\overline{Nu} = 8.504$. CFD with constrained flow gives $\overline{Nu} = 8.723$. CFD with unconstrained flow gives $\overline{Nu} = 9.410$. Experiments⁹ show that $\overline{Nu} = 9.2$. Thus, for the constant heat flux case too, the results obtained by CFD with unconstrained flow are quite close to the experimental value. The average Nusselt numbers predicted by the CFD simulations with constrained velocity are reasonably close to the values given by the similarity analysis, although there can be significant differences in the streamline patterns. The difference is the manifestation of the boundary layer approximations in the similarity analysis. The differences in the fluid flow field and heat transfer characteristics between the two sets of CFD solutions (one with constrained velocity and the other with unconstrained velocity) highlight the influence of the boundary condition imposed at $x = 0$. The two sets of CFD simulations establish, in particular, the conclusion that it is the inappropriateness of the age-old boundary condition $u = 0$ at $x = 0$, and not the boundary layer approximation, that is the principal cause for the vulnerability of the standard similarity analyses (and integral theories) for natural convection.

¹L. C. Burmeister, *Convective Heat Transfer*, 2nd ed. (John Wiley & Sons, New York, USA, 1993).

²W. M. Kays and M. E. Crawford, *Convective Heat and Mass Transfer*, 3rd ed. (McGraw-Hill, New York, USA, 1993).

³J. P. Holman, *Heat Transfer (in SI Units)*, 9th ed. (Tata McGraw-Hill, New Delhi, India, 2008).

⁴H. Schlichting and K. Gersten, *Boundary-Layer Theory*, 8th ed. (Springer, New Delhi, India, 2004).

⁵A. Bejan, *Convection Heat Transfer*, 4th ed. (John Wiley & Sons, New York, USA, 2013).

⁶A. Guha and S. Sengupta, "Effects of finiteness on the thermo-fluid-dynamics of natural convection above horizontal plates," *Phys. Fluids* **28**, 063603-1–063603-29 (2016).

⁷O. A. Saunders, "Natural convection in liquids," *Proc. R. Soc. A* **172**, 55–71 (1939).

⁸M. Fishenden and O. A. Saunders, *An Introduction to Heat Transfer* (Oxford University Press, London, 1950).

- ⁹B. R. Rich and C. Burbank, "An investigation of heat transfer from an inclined flat plate in free convection," *ASME J. Heat Transfer* **75**, 485–499 (1953).
- ¹⁰R. J. Goldstein and E. R. G. Eckert, "The steady and transient free convection boundary layer on a uniformly heated vertical plate," *Int. J. Heat Mass Transfer* **1**, 208–218 (1959).
- ¹¹J. Gryzagoridis, "Natural convection from a vertical flat plate in the low Grashof number range," *Int. J. Heat Mass Transfer* **14**, 162–165 (1971).
- ¹²T. Fuji and H. Imura, "Natural convection heat transfer from a plate with arbitrary inclination," *Int. J. Heat Mass Transfer* **15**, 755–767 (1972).
- ¹³V. E. Schmidt and W. Beckmann, "Das temperatur- und geschwindigkeitsfeld vor einer wärme abgebenden senkrechten platte bei natürlicher konvektion," *Tech. Mech. Thermodynamik* **1**, 391–406 (1930).
- ¹⁴S. Ostrach, "An analysis of laminar free convection flow and heat transfer about a flat plate parallel to the direction of the governing body force," NACA Report 1111, 1953.
- ¹⁵E. M. Sparrow, "Laminar free convection on a vertical plate with prescribed non uniform wall heat flux or prescribed non uniform wall temperature," NACA Tech. Note **3508**, 1–34 (1955).
- ¹⁶L. Lorenz, "Über das wärmeleitvermögen der metalle für wärme und elektrizität," *Weid. Annu. Phys.* **13**, 442–582 (1881).
- ¹⁷E. Pohlhausen, "Der Wärmeaustausch zwischen festen Körpern und Flüssigkeiten mit kleiner Reibung und kleiner Wärmeleitung," *Z. Angew. Math. Mech.* **1**(2), 115–121 (1921).
- ¹⁸T. S. Chen, H. C. Tien, and B. F. Armaly, "Natural convection on horizontal, inclined, and vertical plates with variable surface temperature or heat flux," *Int. J. Heat Mass Transfer* **29**(10), 1465–1478 (1986).
- ¹⁹A. V. Kuznetsov and D. A. Niels, "Natural convective boundary layer flow of a nanofluid past a vertical plate," *Int. J. Therm. Sci.* **49**, 243–247 (2010).
- ²⁰A. Aziz and W. A. Khan, "Natural convective boundary layer flow of a nanofluid past a convectively heated vertical plate," *Int. J. Therm. Sci.* **52**, 83–90 (2012).
- ²¹S. W. Churchill and H. S. Chu, "Correlating equation for laminar and turbulent free convection from a vertical plate," *Int. J. Heat Mass Transfer* **18**, 1323–1329 (1975).
- ²²S. Tieszen, A. Ooi, P. Durbin, and M. Behnia, "Modeling of natural convection heat transfer," in *Proceeding of Summer Program* (Center for Turbulence Research, Stanford University, Stanford, California, 1988), pp. 287–302.
- ²³T. Tsuji and Y. Nagano, "Characteristics of a turbulent natural convection boundary layer along a vertical flat plate," *Int. J. Heat Mass Transfer* **31**, 1723–1734 (1988).
- ²⁴Z. H. Yan and E. A. Nilsson, "Large eddy simulation of natural convection along a vertical isothermal surface," *Int. J. Heat Mass Transfer* **41**, 1004–1013 (2005).
- ²⁵C. S. Ng, A. Ooi, D. Lohse, and D. Chung, "Vertical natural convection: Application of the unifying theory of thermal convection," *J. Fluid Mech.* **764**, 349–361 (2015).
- ²⁶M. Turkyilmazoglu and I. Pop, "Heat and mass transfer of unsteady natural convection flow of some nanofluids past a vertical infinite flat plate with radiation effect," *Int. J. Heat Mass Transfer* **59**, 167–171 (2013).
- ²⁷K. Pradhan and A. Guha, "CFD solutions for magnetohydrodynamic natural convection over horizontal and vertical surfaces," *J. Mol. Liq.* **236**, 465–476 (2017).
- ²⁸A. Guha and S. Samanta, "Effect of thermophoresis and its mathematical models on the transport and deposition of aerosol particles in natural convective flow on vertical and horizontal plates," *J. Aerosol Sci.* **77**, 85–101 (2014).
- ²⁹W. M. Lewandowski, M. Rym, H. Denda, and E. Klugmann-Radziemska, "Possibility of thermal imaging use in studies of natural convection heat transfer on the example of an isothermal vertical plate," *Int. J. Heat Mass Transfer* **78**, 1232–1242 (2014).
- ³⁰D. S. Jain, S. S. Rao, and A. Srivastava, "Rainbow schlieren deflectionometry technique for nanofluid based heat transfer measurement under natural convection regime," *Int. J. Heat Mass Transfer* **98**, 697–711 (2016).
- ³¹A. Guha and K. Pradhan, "A unified integral theory of laminar natural convection over surfaces at arbitrary inclination from horizontal to vertical," *Int. J. Therm. Sci.* **111**, 475–490 (2016).
- ³²B. Gebhart, "Effect of viscous dissipation in natural convection," *J. Fluid Mech.* **14**(2), 225–232 (1962).
- ³³S. Samanta and A. Guha, "A similarity theory for natural convection from a horizontal plate for prescribed heat flux or wall temperature," *Int. J. Heat Mass Transfer* **55**, 3857–3868 (2012).
- ³⁴B. Bradie, *A Friendly Introduction to Numerical Analysis* (Pearson Education, New Delhi, 2007).
- ³⁵Fluent 6.3 User's Guide, Fluent, Inc., Central Source Park, 10 Cavendish Court, Lebanon, NH 03766, USA, 2006.
- ³⁶Y. Mei and A. Guha, "Implicit numerical simulation of transonic flow through turbine cascades on unstructured grids," *Proc. Inst. Mech. Eng., Part A* **219**, 35–47 (2005).
- ³⁷A. Guha and J. B. Young, "Time-marching prediction of unsteady condensation phenomena due to supercritical heat addition," in *Turbomachinery: Latest Developments in a Changing Scene* (Institution of Mechanical Engineers, London, UK, 1991), ISBN: 0852987617.
- ³⁸A. Guha, "Thermal choking due to nonequilibrium condensation," *J. Fluids Eng.* **116**(3), 599–604 (1994).
- ³⁹J. R. Lloyd, E. M. Sparrow, and E. R. G. Eckert, "Laminar, transition and turbulent natural convection adjacent to inclined and vertical surfaces," *Int. J. Heat Mass Transfer* **15**(3), 457–473 (1972).
- ⁴⁰P. E. Dimotakis, "The mixing transition in turbulent flows," *J. Fluid Mech.* **409**, 69–98 (2000).
- ⁴¹A. Guha and S. Samanta, "Closed-form analytical solution for laminar natural convection on horizontal plates," *ASME J. Heat Transfer* **135**(10), 102501-1–102501-9 (2013).